Journal of Thermal Science Vol.31, No.6 (2022) 2293−2308

https://doi.org/10.1007/s11630-022-1711-9 **Article ID: 1003-2169(2022)06-2293-16**

Numerical Investigation on Pool Boiling Mechanism of Hybrid Structures with Metal Foam and Square Column by LBM

LIU Zhongyi, QIN Jie, WU Ziheng, YUE Sijia, XU Zhiguo*

School of Mechanical Engineering, Shanghai Jiao Tong University, Shanghai 200240, China

Abstract: In the present study, pool boiling heat transfer performance and bubble behaviors of hybrid structures with metal foam and square column are investigated by lattice Boltzmann method. By using the vapor-liquid phase change model of Gong-Cheng and Peng-Robinson equation of state, the effects of structural parameters, including metal foam thickness, porosity, column height and ratio of column width (W) to gap spacing (D) are investigated in details. The results show that hybrid structure performs better than pure columnar structure in pool boiling heat transfer. The hybrid structure accelerates bubble growth by fluid disturbance while metal skeletons prevent the bubble escaping. The optimum ratio of column width to gap spacing decreases with the increase of heat flux and HTC (heat transfer coefficient) can achieve an increase up to 25% when W/D change from 5/3 to 1/3. The increase of column height enhances heat transfer by expanding surface area and providing space for bubble motion. The metal foam thickness and porosity have a little influence on pool boiling heat transfer performance, but they have an important effect on bubble motion in the regime.

Keywords: hybrid structure, metal foam, square column, pool boiling heat transfer, lattice Boltzmann method

1. Introduction

Due to the high heat transfer efficiency and low superheat, pool boiling has been widely used in industrial fields, such as steam generators, chip cooling, etc. Various measures have been taken to improve the boiling heat transfer performance, which can be divided into two categories. One is changing the characteristics of working medium [1], such as adopting different fluid [2, 3] and adding other activators in the fluid [4–7]. The other is adding strengthened structures on the surface to extend surface area [8] and enhance fluid disturbance [9], such as porous coated surface [10–12], micro and mini finned surface [13–15], pitted surface [16], microchannels [17, 18]. As for structure modification, micro columnar surface has high heat transfer coefficient (HTC) due to its high thermal conductivity and surface area. However, the column hinders the replenishment of fresh liquid to the boiling surface and results in low critical heat flux (CHF). In contrast, for porous metal foam, its application in the regime that requires fast thermal response is restricted due to low effective thermal conductivity, but it has many inner-connected pores serving as nucleation sites, and its porous structure has strong capillary force which is conducive to the fresh liquid supplement.

Nowadays, researchers are focusing on hybrid surface modification to combine the advantages of different strengthened structures [19]. Xu et al. [20] studied the effect of the combination of porous metal foam and

Received: Nov 08, 2020
AE: KIM Heuy-Dong

Corresponding author: XU Zhiguo E-mail: zhiguoxu@sjtu.edu.cn

Nomenclature

A	Surface area	t	Time
c	Lattice speed	$\boldsymbol{U}$	Real fluid velocity vector
c_s	Lattice sound speed	$\boldsymbol{u}$	Velocity vector
D	Gap spacing between two column	W	Width of the column
D_0	Bubble departure diameter	$\boldsymbol{x}$	Lattice position vector
$\boldsymbol{e}_i$	Lattice velocity vector	**Greek symbols**	
$\boldsymbol{F}$	Body force	α	Thermal diffusivity
f	Bubble departure frequency	β	Weighting factor
f_i, g_i	Distribution function	γ	Ratio of thermal mass of solid and fluid
f_i^{eq} , g_i^{eq}	Equilibrium distribution function	ε	Metal foam porosity
G_{int}	Interaction strength function	ρ	Density
g	Interaction strength	σ	Surface tension
$\boldsymbol{g}$	Gravity acceleration	τ	Relaxation time
H	Height of the column	υ	Kinematic viscosity
H_b	Height of the heater	Φ	Source term
i	Direction	ψ	Pseudopotential function
L_b	Width of the heater	ω	Acentric factor
L_x	Width of the fluid domain	**Subscripts**	
L_y	Height of the fluid domain	ave	Average
n	Metal foam thickness	c	Critical
p	Pressure	int	Interparticle
q	Heat flux	l	Liquid
R_b	Bubble radius	s	Solid
r	Capillary size	sat	Saturation
T	Temperature	v	Vapor

micro-channels on pool boiling heat transfer performance, and found that U-shaped grooves, V-shaped grooves, unidirectional channels, and hybrid cross-channels on the surface of metal foam accelerate vapor-liquid phase change significantly. Pastuszko [21] conducted experiments to compare the heat transfer performance of micro-fin structures with and without wire meshes, studied the heat transfer phenomenon and obtained the optimal parameters of the foil. Jaikumar and Kandlikar [22, 23] deposited porous coatings on the surface of the microchannel, the top of the fin and the wall of the channel to study the pool boiling heat transfer mechanism and three corresponding strengthening mechanisms have been identified. They found that the porous coating on the top of the microchannel provides nucleation sites, and the microconvection heat transfer mechanism is formed in the microchannel and significantly enhances HTC. The combination of the two enhancement technologies ultimately led to the improvement of CHF.

However, due to the limitations of observation techniques, the visualization of the internal flow field is difficult to achieve. Nowadays, numerical simulation methods are applied to explore the heat transfer mechanism and characteristics on the structured surface during pool boiling. As a mesoscopic method, lattice Boltzmann method (LBM) is a powerful tool for multiphase flow simulation and solves the topological evolution of the vapor-liquid interface during bubble coalescence and split successfully. It has a more clear formula than Navier-Stokes equation, which is easy to implement and compatible with parallelization. In addition, the calculation cost of LBM is lower than traditional molecular dynamics simulation. Gong and Cheng [24, 25] proposed an improved vapor-liquid phase change lattice Boltzmann (LB) model and studied the nucleation process of boiling heat transfer bubbles in saturated pool boiling, the effect of surface wettability on the heat transfer coefficient, CHF and horizontal surface boiling curve was also investigated. Chang et al. [26] studied the pool boiling heat transfer enhancement on columnar structure surface by LBM. The effects of geometric parameters such as column height (H), column width (W) and gap spacing (D) were discussed in details.

They found that the heat transfer performance mainly depends on the expanded surface area (A) and local convective flow field. Zhou et al. [27, 28] studied the effect of cavity shape on bubble growth and diffusion by LBM, and further studied the periodic bubble behaviors on the surface of the micro-pillar structure. They found that micro structure accelerates the fluid nucleation, and the geometry of the micro-pillar affects bubble growth significantly. The decrease of column height increases the heat flux in the regime and decreases the bubble departure period. While the gap spacing decides the time of nucleate site formation. Compared with numerous experimental studies [29, 30], there are fewer simulation studies on metal foam structures. One main reason is the lack of physical model to describe the heat and mass transfer process among metal foams properly, and researchers have been trying to solve this problem. Krishnan et al. [31] proposed a three-dimensional polyhedron periodic element model. Boomsma and Poulikakos [32] proposed a one-dimensional heat conduction model based on the three-dimensional forty-two-sided frame of the metal foam. Calmidi et al. [33] treated the porous structure as a two-dimensional array of hexagonal cells, and raised a one-dimensional heat conduction model. Based on Calmidi's model, Qin et al. [34] proposed a 2D open-cell foam metal reconstruction model for LBM simulation, and considered the thermal response of the metal foam.

According to the researches above, for hybrid structures, most experiments focus on the overall heat transfer performance due to the non-visualization of bubble behaviors inside; besides, the final results may be influenced by other factors during the experiment, which makes it hard to study the pool boiling heat transfer mechanism of hybrid structure experimentally. While numerical simulation can achieve the observation of bubble phenomenon and eliminate the interference of other factors, it is a good choice for hybrid structure investigation theoretically. However, most simulations were focused on simple protrusion structures such as pit, column, metal foam and so on. Column and metal foam are normal strengthened structures. Their combination may take full use of their own advantages and lead to new pool boiling mechanism different from the single structure, so it is necessary to explore pool boiling heat transfer process of hybrid structure with column and metal foam. In the present study, the vapor-liquid phase change model of the Gong-Cheng LBM [21] and the Peng-Robinson equation of state (P-R EOS) are used to study the pool boiling of hybrid structures with square column and metal foam. The effects of ratio of column width to gap spacing (W/D), metal foam porosity (ε) and thickness (n) on the heat transfer performance are investigated, and the bubble behaviors and pool boiling heat transfer mechanism in the hybrid structures are revealed.

2. Methodology Model Description

Two particle distribution functions, including the density distribution function for the multiphase LBM model and the temperature distribution function for the energy equation model, are applied to simulate the phase change process in this method.

2.1 The modified pseudo-potential LBM model for multiphase flows

The evolution equation of the density distribution function is governed by:

$$\begin{aligned} & f_i\left(\boldsymbol{x}+\boldsymbol{e}_i\delta_{\mathrm{t}},t+\delta_{\mathrm{t}}\right)-f_i\left(\boldsymbol{x},t\right) \\ &=-\frac{1}{\tau}\left[f_i\left(\boldsymbol{x},t\right)-f_i^{\mathrm{eq}}\left(\boldsymbol{x},t\right)\right]+\Delta f_i\left(\boldsymbol{x},t\right) \end{aligned} \tag{1}$$

where $f_i(\boldsymbol{x},t)$ is the particle distribution function of a particle with velocity $\boldsymbol{e}_i$ at time t and position $\boldsymbol{x}$, and τ is the relaxation time. $f_i^{\mathrm{eq}}(\boldsymbol{x},t)$ is the corresponding equilibrium distribution function. $\Delta f_i(\boldsymbol{x},t)$ is the body force. Equilibrium distribution function is given by:

$$f_i^{\mathrm{eq}}\left(\boldsymbol{x},t\right)=\omega_i\rho\left[1+\frac{\boldsymbol{e}_i\cdot\boldsymbol{u}}{c_{\mathrm{s}}^2}+\frac{\left(\boldsymbol{e}_i\cdot\boldsymbol{u}\right)^2}{2c_{\mathrm{s}}^4}-\frac{\boldsymbol{u}^2}{2c_{\mathrm{s}}^2}\right] \tag{2}$$

where ω_i is the weighting coefficients; $\boldsymbol{u}$ is the velocity and c_{s} is the lattice sound speed.

$$c_{\mathrm{s}}^2=c^2/3 \tag{3}$$

Body force term is given by:

$$\Delta f_i\left(\boldsymbol{x},t\right)=f_i^{\mathrm{eq}}\left[\rho\left(\boldsymbol{x},t\right),\boldsymbol{u}+\Delta\boldsymbol{u}\right]-f_i^{\mathrm{eq}}\left[\rho\left(\boldsymbol{x},t\right),\boldsymbol{u}\right] \tag{4}$$

with $\Delta\boldsymbol{u}$ being the velocity change caused by the body force during time step δ_{t}. The body force $\boldsymbol{F}$ is composed by interparticle interaction force $\boldsymbol{F}_{\mathrm{int}}$, interaction force between fluid and solid $\boldsymbol{F}_{\mathrm{s}}$ and gravity force $\boldsymbol{F}_{\mathrm{g}}$.

$$\boldsymbol{F}\left(\boldsymbol{x}\right)=\boldsymbol{F}_{\mathrm{int}}\left(\boldsymbol{x}\right)+\boldsymbol{F}_{\mathrm{s}}\left(\boldsymbol{x}\right)+\boldsymbol{F}_{\mathrm{g}}\left(\boldsymbol{x}\right) \tag{5}$$

$\boldsymbol{F}_{\mathrm{int}}$ is given by:

$$\begin{aligned} \boldsymbol{F}_{\mathbf{int}}\left(\boldsymbol{x}\right)=&-\beta\psi\left(\boldsymbol{x}\right)\sum_{\boldsymbol{x}'}G_{\mathrm{int}}\left(\boldsymbol{x},\boldsymbol{x}'\right)\psi\left(\boldsymbol{x}'\right)\left(\boldsymbol{x}'-\boldsymbol{x}\right) \\ &-\frac{1-\beta}{2}\sum_{\boldsymbol{x}'}G_{\mathrm{int}}\left(\boldsymbol{x},\boldsymbol{x}'\right)\psi^2\left(\boldsymbol{x}'\right)\left(\boldsymbol{x}'-\boldsymbol{x}\right) \end{aligned} \tag{6}$$

where G_{int} is the interparticle interaction strength; β is related to the equation of state used in the simulation, and $\psi(\boldsymbol{x})$ is a function of the local density and determined by the equation of state, which is given by:

$$\psi\left(\boldsymbol{x}\right)=\sqrt{\frac{p-\rho c_{\mathrm{s}}^2}{3\boldsymbol{g}}} \tag{7}$$

In this article, we adopt the P-R EOS. The pressure p is given by:

$$p=\frac{\rho RT}{1-b\rho}-\frac{a\rho^2\varepsilon(T)}{1+2b\rho-b^2\rho^2} \tag{8}$$

$$\varepsilon(T)=\left[1+\left(0.374\ 64+1.546\ 62\omega-0.269\ 92\omega^2\right)\left(1-\sqrt{T/T_c}\right)\right]^2 \tag{9}$$

with ω being the acentric factor and is chosen as 0.344. a=9/42, b=2/21, R=1.

$\boldsymbol{F}_s$ is given by:

$$\boldsymbol{F}_s=-\varphi(\boldsymbol{x})\sum_{\boldsymbol{x}'}G_s(\boldsymbol{x},\boldsymbol{x}')s(\boldsymbol{x}')\boldsymbol{e}_i \tag{10}$$

where G_s is the fluid-solid interaction strength of adjusting the contact angles. $s(\boldsymbol{x})$ is the indictor function, which is used to justify whether the node $\boldsymbol{x}$ is in solid or in fluid.

$\boldsymbol{F}_g$ is given by:

$$\boldsymbol{F}_g=\left[\rho(\boldsymbol{x})-\rho_{ave}\right]\boldsymbol{g} \tag{11}$$

where ρ_{ave} is the average density of the whole computation domain; $\boldsymbol{g}$ is the acceleration of gravity.

2.2 Energy equation model

The modified evolution equation of temperature distribution is given by:

$$g_i(\boldsymbol{x}+\boldsymbol{e}_i\delta_t,t+\delta_t)-g_i(\boldsymbol{x},t)=-\frac{1}{\tau_T}\left[g_i(\boldsymbol{x},t)-g_i^{eq}(\boldsymbol{x},t)\right]+\delta_t\omega_i\Phi \tag{12}$$

where $g_i(\boldsymbol{x},t)$ is the temperature distribution function; τ_T is the dimensionless relaxation time for temperature; $g_i^{eq}(\boldsymbol{x},t)$ is the equilibrium distribution function for temperature; Φ is the source term.

The equilibrium temperature distribution function is given by:

$$g_i^{eq}(\boldsymbol{x},t)=\omega_i T\left[1+\frac{\boldsymbol{e}_i\cdot\boldsymbol{U}}{c_s^2}+\frac{(\boldsymbol{e}_i\cdot\boldsymbol{U})^2}{2c_s^4}-\frac{\boldsymbol{U}^2}{2c_s^2}\right] \tag{13}$$

The source term in the energy equation is:

$$\Phi=T\left[1-\frac{1}{\rho c_v}\left(\frac{\partial p}{\partial T}\right)_\rho\right]\nabla\cdot\boldsymbol{U} \tag{14}$$

where C_v is the specific heat capacity of vapor; $\boldsymbol{U}$ is the real velocity of the fluid.

A D2Q9 scheme is chosen for 2D simulations in this study. And the discrete velocity vectors are:

$$\boldsymbol{e}_i=\begin{cases}(0,0) & i=0\\ c\left[\cos\left(\frac{i-1}{2}\pi\right),\sin\left(\frac{i-1}{2}\pi\right)\right] & i=1-4\\ \sqrt{2}c\left[\cos\left(\frac{2i-9}{4}\pi\right),\sin\left(\frac{2i-9}{4}\pi\right)\right] & i=5-8\end{cases} \tag{15}$$

The corresponding weighting coefficients are given by:

$$G_{int}(\boldsymbol{x},\boldsymbol{x}')=\begin{cases}2g_{int} & |\boldsymbol{x}'-\boldsymbol{x}|=1\\ g_{int}/2 & |\boldsymbol{x}'-\boldsymbol{x}|=\sqrt{2}\\ 0 & \text{otherwise}\end{cases} \tag{16}$$

$$G_s(\boldsymbol{x},\boldsymbol{x}')=\begin{cases}2g_s & |\boldsymbol{x}'-\boldsymbol{x}|=1\\ g_s/2 & |\boldsymbol{x}'-\boldsymbol{x}|=\sqrt{2}\\ 0 & \text{otherwise}\end{cases} \tag{17}$$

where g_{int} is the fluid-fluid interaction strength and g_s is the solid-fluid interaction strength which is determined by the contact angles.

The relaxation time τ and τ_T are connected to kinematic viscosity υ and thermal diffusivity α:

$$\tau=\frac{\upsilon}{c_s^2\delta_t}+\frac{1}{2} \tag{18}$$

$$\tau_T=\frac{\alpha}{c_s^2\delta_t}+\frac{1}{2} \tag{19}$$

Other factors like ρ, $\boldsymbol{u}$, $\boldsymbol{U}$ and T are updated after every collision-diffusion time-step, which are given by:

$$\rho=\sum_i f_i \tag{20}$$

$$\rho\boldsymbol{u}=\sum_i \boldsymbol{e}_i f_i \tag{21}$$

$$\rho\boldsymbol{U}=\rho\boldsymbol{u}+\delta_t/2 \tag{22}$$

$$T=\sum_i g_i \tag{23}$$

3. Model Validation and Computational Domain

3.1 Model validation

3.1.1. P-R equation validation

To validate the present model, the coexistence curve of P-R EOS is simulated numerically. A 2D computational domain with a 100×100 (lattice unit. The length units mentioned in the article are all lattice units.) grid system is adopted and periodic boundary condition is applied at all sides of computational domain. The

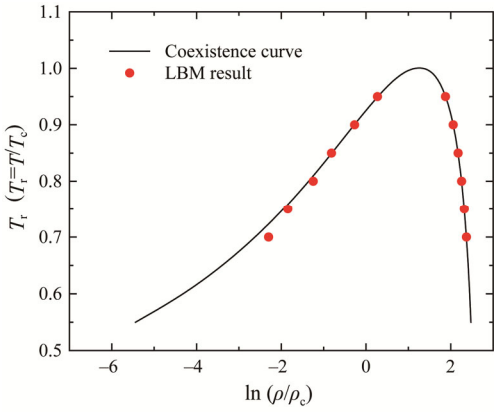

Fig. 1 Coexistence curve

domain is full of fluid at a density lower than ρ_c, while a droplet with a density slightly higher than ρ_c is set at the central domain. The simulation results at the steady state are compared with analytical results obtained by Maxwell construction and are shown in Fig. 1, which agree well with analytical solutions.

3.1.2 Bubble departure diameter and frequency validation

According to the static force balance of adhesive force and buoyant force, the correlation between the bubble departure diameter and gravity was proposed by Fritz [35]:

$$D_0 = \sqrt{\frac{\sigma}{\boldsymbol{g}\left(\rho_l - \rho_v\right)}} \tag{24}$$

And the relation between the bubble departure frequency and gravity was raised by Zuber [36]:

$$f^{-1} \sim D_0 \left[\frac{\sigma \boldsymbol{g}\left(\rho_l - \rho_v\right)}{\rho_l^2}\right]^{-0.25} \tag{25}$$

To validate the function $D_0 \sim \boldsymbol{g}^{-0.5}$ and $f^{-1} \sim \boldsymbol{g}^{-0.75}$, the model shown in Fig. 2 is adopted to explore the relationship between bubble departure diameter and gravitational acceleration. The numerical results are presented in Fig. 3. The exponent of the $\boldsymbol{g} \sim D_0$ fitting curve of our numerical results is –0.517, and the exponent of the $\boldsymbol{g} \sim f$ fitting curve of our numerical results is –0.750, which agree well with the correlation given by Fritz et al. and Zuber et al. respectively.

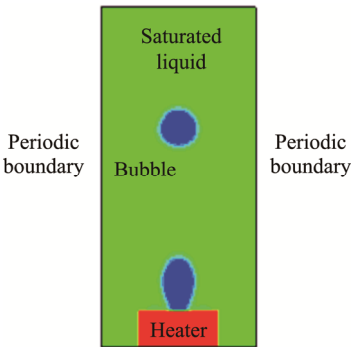

Fig. 2 Validation model

3.2 Computational domain, initial conditions and boundary conditions

In this section, pool boiling heat transfer on a typical structured surface with hybrid structure is studied. The 2D computational mesh size is $L_x \times L_y = 640 \times 500$, with a heater grid size of $L_b \times H_b = 640 \times 100$. The schematic diagram is shown in Fig. 4. The solid substrate with hybrid structure is located at the bottom of the domain, which is composed of two parts. The upper part is the metal foam structure, while the below part is the micro

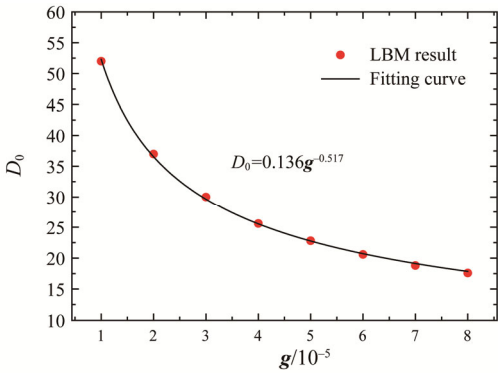

(a) Bubble departure diameter

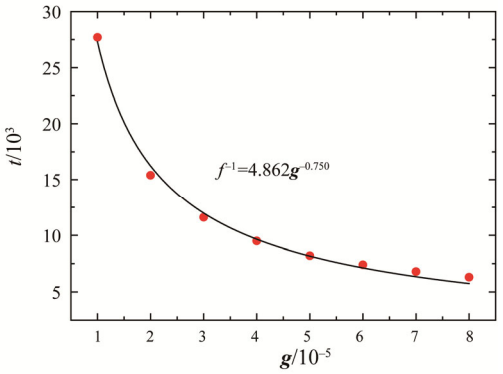

(b) Bubble departure frequency

Fig. 3 Gravity effects

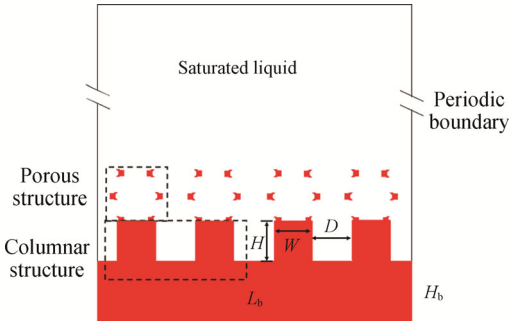

Fig. 4 Schematic of the computational domain

columns. The metal foam is characterized by porosity and thickness. Columns are featured by column width W, gap spacing D, and height H. Initially, the fluid region is fully occupied by saturated liquid. Constant heat flux boundary condition is applied in the solid bottom, and the constant temperature and pressure boundary condition are imposed on the upper boundary of the computational domain. Periodic boundary condition is applied on the left and right boundaries. At the fluid-solid interface, the conjugate heat transfer method posted by Li et al. [37] is adopted and given by:

$$g_i\left(\boldsymbol{x}_f, t+\delta_t\right) = \frac{1-\gamma}{1+\gamma} g_i\left(\boldsymbol{x}_f, t\right) + \frac{2\gamma}{1+\gamma} g_{i^-}\left(\boldsymbol{x}_s, t\right) \tag{26}$$

$$g_i\left(\boldsymbol{x}_s, t+\delta_t\right) = -\frac{1-\gamma}{1+\gamma} g_{i^-}\left(\boldsymbol{x}_s, t\right) + \frac{2}{1+\gamma} g_i\left(\boldsymbol{x}_f, t\right) \tag{27}$$

where, $\bar{i}$ is the reverse direction of i. γ is the ratio of thermal mass of solid and fluid:

$$\gamma=\left(\rho c_p\right)_s/\left(\rho c_p\right)_f \tag{28}$$

Other factors such as kinematic viscosity and specific heat are all listed in the nomenclature.

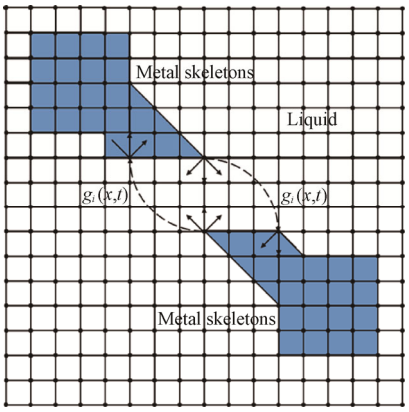

Fig. 5 Heat transfer among porous nodes

Table 1 Physical properties adopted in the simulations (lattice units)

	Solid	Liquid	Vapor
Density (ρ)	23.6	5.9	0.58
Specific heat (c_p, c_v)	1	4	2
Thermal diffusion coefficient (α)	2	0.095	0.10

The reconstructed model raised by Qin et al. [34] is adopted in the construction of metal foams. To simulate the continuity of pores in reality, the connections of ligaments are considered as quadrate nodes and the channels function as the connections among cells. The schematic of the thermal conduction among discrete metal skeleton is shown in Fig. 5. The temperature information of discrete solid blocks is transferred through the channels, and the adiabatic boundary is applied between the virtual nodes and its sounding liquid nodes to achieve energy conservation.

4. Results and Discussion

4.1 Comparison of different structured surface

In the present study, simulations are carried out on a micro columns structure and a hybrid structure with micro columns and metal foam. The spacing between two columns is fixed as 160. The column is chosen to be $L_b\times W\times D$=60×80×80, and the porosity of the metal foam is 0.94. The structured surfaces are shown in Fig. 6.

Fig. 7 shows the boiling curves in terms of heat flux versus dimensionless T^* under controlled wall heat flux condition of the two structures. T^* is given by:

$$T^*=\left(T_w-T_{sat}\right)/T_c \tag{29}$$

where T_w is the temperature of the liquid-solid surface; T_{sat} is the temperature of the saturated liquid; T_c is the critical temperature. It can be seen from Fig. 7 that pool boiling heat transfer performance of the hybrid structure is better than the pure column structure. Besides, there are turning points at the heat flux (q) of 0.0024, which means the approach of CHFs.

Fig. 8 shows the typical bubble behaviors during the nucleate boiling. Bubbles generate from the center of channels at first (t=13 200), and then at the feet of the columns (t=18 000). As time goes by, more nucleation sites are activated (t=24 400). Compared to situation of the columnar structure surface, the hybrid structure has a larger heated surface area. What's more, the existence of metal foam on the top of columns causes more severe disturbance and provides capillary force in the field. According to Young-Laplace equation, the capillary pressure is given by:

$$\Delta p_c=\frac{2\sigma\cos\theta}{r} \tag{30}$$

where σ is the surface tension and r is the capillary size. Since the metal foam is hydrophilic, the capillary force promotes the liquid and bubbles flow inside pores, which plays a key role in heat transfer enhancement. To make use of the capillary force, the surface is set as hydrophilic, which means the static contact angle is an acute angle.

Fig. 9(b) shows the partial flow field in nucleate boiling regime with hybrid structure at q=0.0016. The

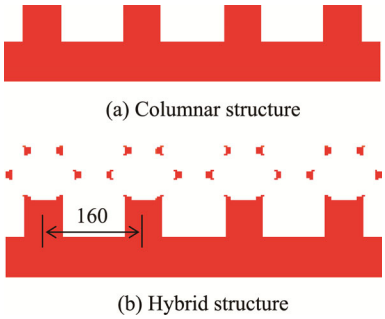

(a) Columnar structure

(b) Hybrid structure

Fig. 6 Different structured surface

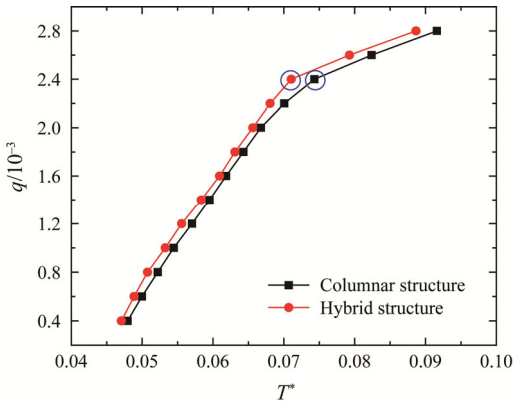

Fig. 7 Pool boiling heat transfer curve

(a) t=13 200 (b) t=18 000 (c) t=24 400

Fig. 8 Bubble behaviors (q=0.0024)

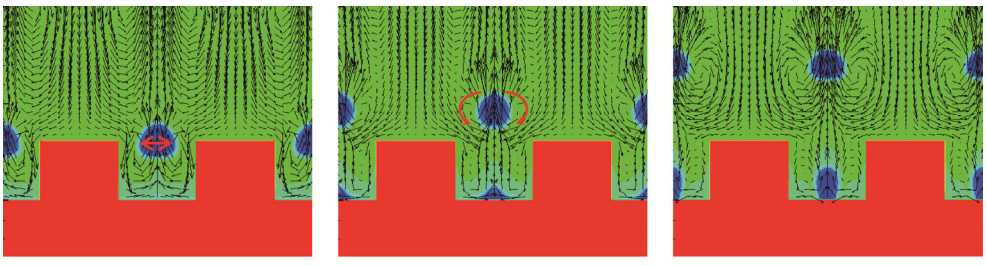

t=45 200 t=47 200 t=49 200

(a) Columnar structure

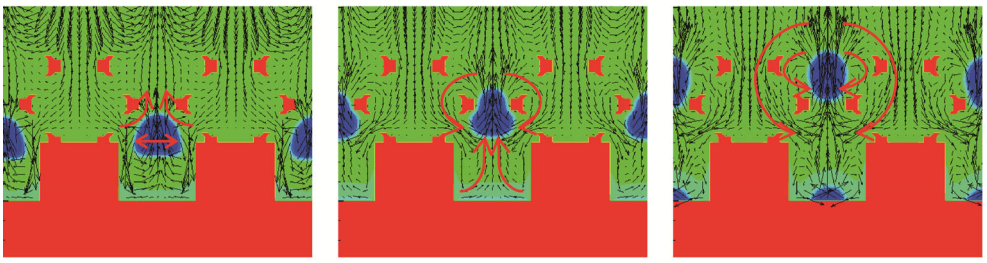

t=45 200 t=47 200 t=49 200

(b) Hybrid structure

Fig. 9 Flow field (q=0.0016)

flow field differs from that of the columnar surface (Fig. 9(a)) in the following three aspects. Firstly, the presence of metal skeletons violates the fluid flow, which accelerates the heat transfer among fluid. The bubble in Fig. 9(b) is bigger than bubbles in Fig. 9(a) due to better heat transfer enhancement. Secondly, there is convection in the pore of metal foam; liquid is heated in the pores and would bring the heat to the whole field. Thirdly, when a bubble rises to the interface of column and metal foam, there is convective vortex in the channel of surrounding metal skeletons as well as on the both side of the bubble.

4.2 Ratio of column width to gap spacing effect

The strengthening effect of the hybrid structure is affected by morphologies of column and metal foam, such as column width, column spacing, porosity of the metal foam and so on. The simulation is carried out by changing the ratio of column width to gap spacing (W/D), column height (H) and porosity (ε) of the hybrid structure respectively. The simulation parameters are shown in Table 2.

Table 2 Physical properties adopted in the simulations

Case	W	D	H	n	ε
1	100	60	60	1	0.94
2	80	80	60	1	0.94
3	60	100	60	1	0.94
4	40	120	60	1	0.94
5	80	80	20	1	0.94
6	80	80	100	1	0.94
7	60	100	60	1	0.90
8	60	100	60	1	0.96
9	80	80	20	2	0.94
10	80	80	20	3	0.94

In this section, the effect of W/D is discussed. The spacing between two columns is fixed as 160 to keep the heat transfer area of hybrid structure unchanged. The increase of W/D means a larger column width and a smaller column spacing. The larger the W, the higher the ribbed efficiency and the more heat can be transferred to the fluid in the field. However, the smaller the D, the

narrower the bubble growth space and the greater the bubble motion resistance. Fig. 10 shows pool boiling heat transfer performances of four hybrid structures with W/D ratios of 5/3, 1/1, 3/5, 1/3, respectively, while H=60, ε=0.94, n=1. The difference of heat transfer enhancement among structures varies with heat flux. q=0.001 is a turning heat flux. When q<0.001, the heat transfer performance of W/D=5/3, 1/1, 3/5 is almost the same, but the structure with W/D=1/3 is inferior to the other three structures with a HTC reduction of 0.15%–3.4%. The reason is the least contact area between column and metal foam. When 0.001<q<0.0024, it can be found that with the increase of heat flux, the hybrid structure with a higher W/D ratio tends to have worse heat transfer performance due to the narrower channel wall and higher bubble escaping resistance. When W/D is reduced from 5/3 to 1/3, the HTC can increase up to 25%. Besides, the CHF of the hybrid structure with the ratio of 5/3 reaches

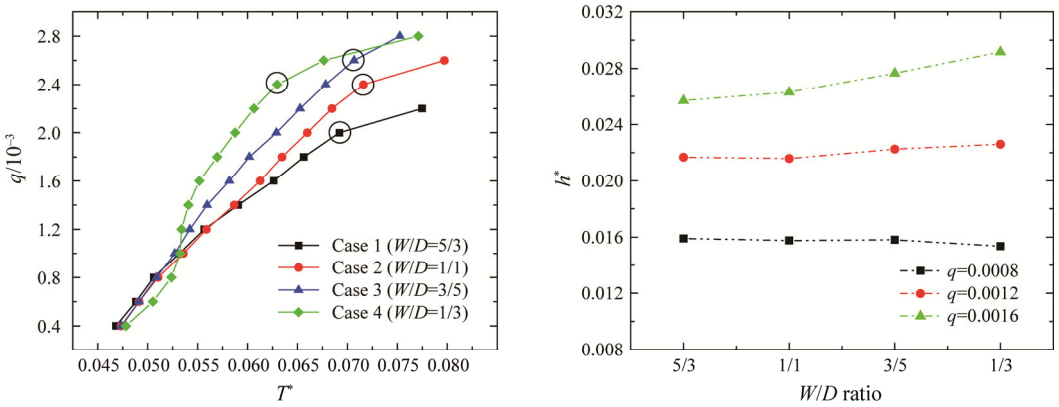

(a) Pool boiling curves (b) Pool boiling heat transfer coefficients

Fig. 10 Ratio of column width to spacing effect on pool boiling curves

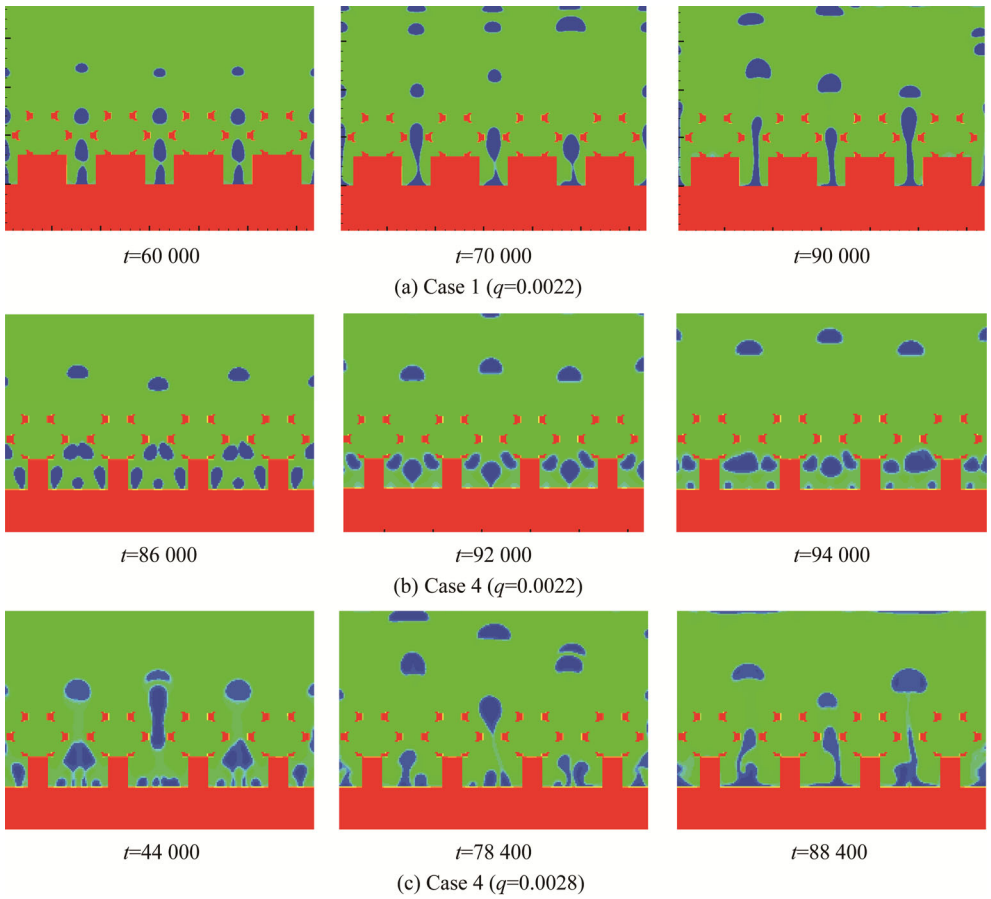

(a) Case 1 (q=0.0022)

(b) Case 4 (q=0.0022)

(c) Case 4 (q=0.0028)

Fig. 11 Bubble behaviors in Case 1 and Case 4

earlier than the others (q=0.0020), because the counterflow between escaping bubbles and replenishing fresh liquid happens more easily in a narrower channel. Fig. 11(a) shows the bubble behaviors of W/D=5/3 at transition boiling regime. For W/D=5/3, there is only one nucleation site in a channel, and bubble rises and crosses the metal skeletons. As time goes by, bubbles merge and are stretched into bubble strings. During the ascent process, bubble strings are heated by the channel bottom and metal skeletons, then they become bigger and their departure are difficult. Since the channel bottom is covered by vapor, the heat transfer between the liquid and the bottom heating surface is restricted.

Fig. 11(b) shows the bubble behaviors for W/D=1/3 at nucleate boiling. It can be seen that three nucleation sites are activated in the channel bottom (t=86 000), and there is enough space for bubble departure, deformation, sliding, and coalescence (t=92 000). The channels are wide and can always be in contact with the cooling liquid, which attributes to heat transfer performance. When the bubbles rise to the contact interface between the top of the square column and the metal foam, they are hindered by the metal foam, and the bubbles gather and merge (t= 94 000). Fig. 11(c) shows the bubble behaviors for W/D= 1/3 at transition boiling. While many bubbles generate at a high heat flux, they don't detach completely, but leave a small bubble on the wall to become a new nucleation site, then four nucleation sites are activated in a single channel (t=44 400). The adjacent bubbles on the wall merge together (t=78 400). With the extension of the heating time, a large number of bubbles deform, slide and coalesce on the wall surface, then fuse and form a vapor film (t=88 400), thus deteriorate the heat transfer. Besides, Fig. 11 also shows that escaping bubbles are decelerated by the metal skeletons.

4.3 Column height effect

Fig. 12 shows the boiling curves of hybrid structure with different column height H for the fixed W/D ratio (1/1) and metal foam porosity (ε=0.94). Column height ranges from 20 to 100. The specific parameters are shown in Table 2. It can be found that the heat transfer performance increases with increasing column height when q<0.002 because of a larger surface area, which is consistent with the simulation results of Chang et al [26]. Fig. 13 shows the average dimensionless temperature variation with time-step on the surface (y=H) at q= 0.0012. A lower H leads to a higher average wall temperature and smaller fluctuation range. When H increases from 60 to 100, the difference between the two temperature variations is not obvious. Results suggest that at a low heat flux, the increase of H has no obvious effect on the value of temperature and bubble departure period after a certain H.

The bubble behavior of three cases at q=0.0020 are shown in Fig. 14. The lower the columns, the smaller the bubble grows in the channels. And a low H also means a

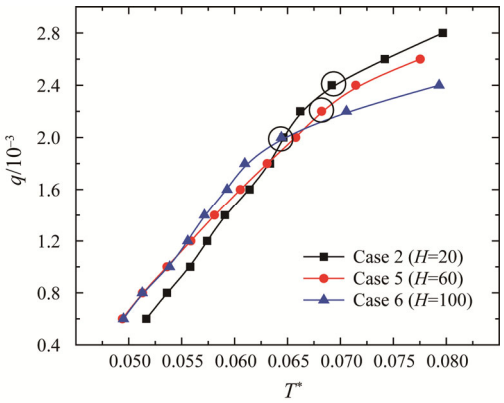

Fig. 12 Column height effect on pool boiling curves

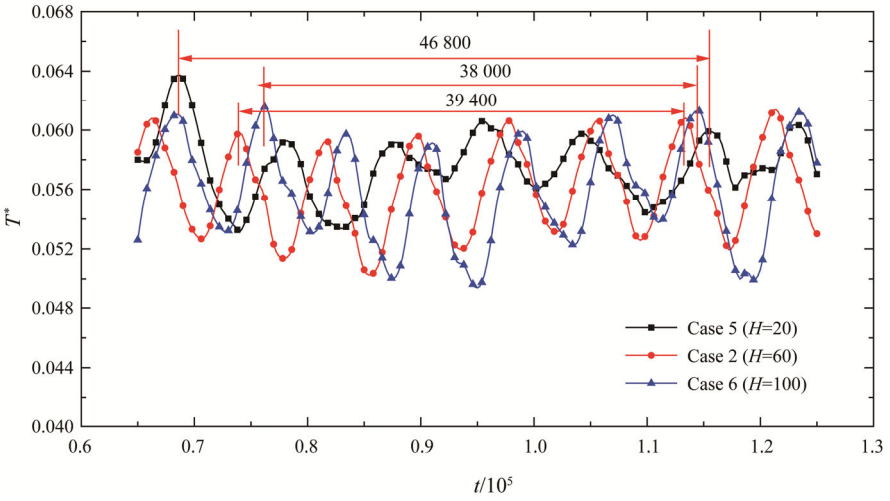

Fig. 13 Bubble behaviors for different H (t=90 000, q=0.0012)

high possibility for bubbles to escape. It is found that the bigger bubbles generated in a channel with a higher H are difficult to cross the metal skeletons at the high heat flux (Fig. 14), which results in higher bubble escaping resistance. Fig. 15 presents dimensionless temperature distribution along the solid horizontal interface for hybrid structures in Fig. 14. The black dash dot lines mark the junction of column and heat wall. It is noted that a lower H is attributed to a higher temperature on the top of columns, which explains the bubble generation on the top of columns in Fig. 14(a) and is accompanied by temperature reduction. For the channel bottom, the temperature on the central zone is lower than lateral zone due to the latent heat transferred by bubbles. For H=20, the temperature on the channel bottom is lower than that in the column, which implies the phase change heat transfer is stronger than heat conduction inside the solid. Due to the increase of nucleation sites on the top of columns and small bubble escaping resistance in the channels, hybrid structure achieves better heat transfer performance at a lower H when q>0.002.

Besides, Fig. 12 also shows that a larger CHF is achieved at a lower H, which is contrary to Chang et al. [26]. This is because CHF of columnar structure is only affected by the surface area. However, for the hybrid structures in the present study, the metal skeletons play an important role in the bubble nucleation and escaping. Fig. 16 shows the comparison of bubble behavior of H=20 and H=100 when q=0.0024. It can be seen from Fig. 16(a) that when at a high heat flux, two nucleation sites will be activated at the channel bottom of H=20 at the same time, then two adjacent bubbles will merge into one on the wall, continue to grow into a big bubble. The growth space of the bubbles is squeezed because of the close connection to upper metal skeleton. The growth force of the bubbles and the capillary force of the metal skeletons promote bubbles to pass through the metal skeletons, leaving a small segment of bubbles on the wall. The remaining bubbles merge with the newly nucleated bubbles to start a new bubble cycle. At the same time, it can be noticed that there are small bubbles generated from the top of the column, and are heated during the process of passing through the metal skeletons; the bubbles become smaller and even evaporated. The increase of nucleation sites and the rapid detachment of bubbles postpone the CHF point of H=20. Fig. 16(b) shows the bubble behavior of Case 6 when q=0.0024. As we mentioned before, the temperature on a highest fin top becomes too low to sustain boiling, so it provides no additional heat transfer enhancement. Bubbles generating in H=100 will merge, grow and detach in the channel just as H=20. The difference is that the two nucleation sites in

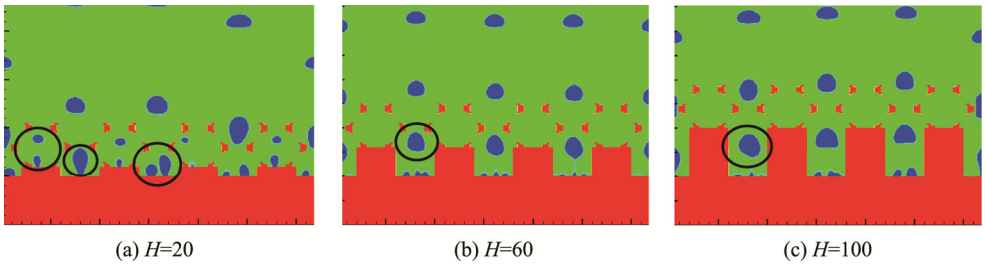

(a) H=20 (b) H=60 (c) H=100

Fig. 14 Temperature variation with time-step on the surface (y=H, q=0.0020)

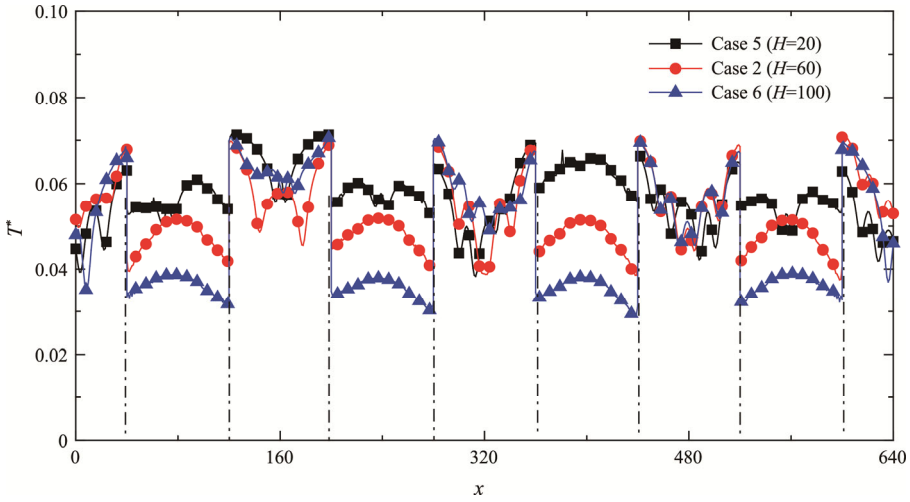

Fig. 15 Temperature distribution along the solid horizontal interface

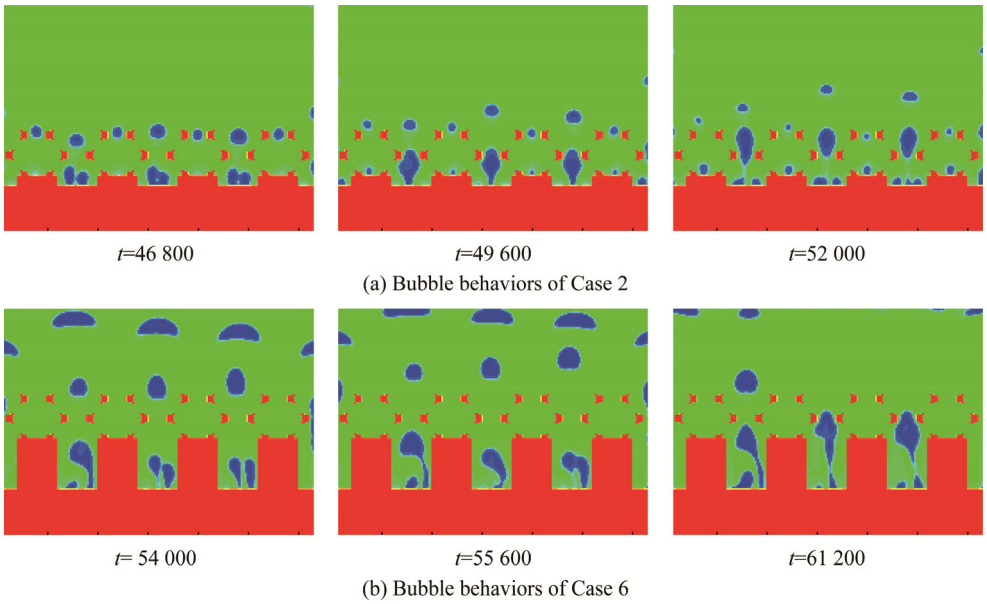

Fig. 16 Comparison of bubble behaviors in Case 2 and Case 6 (q=0.0024)

a channel are activated one after another. One bubble detaches first, and merges with the bubble at the corner during the detachment process. Heated by the wall, the bubble continues to elongate in the channel. When it rises below the metal skeletons, it is sucked into the skeletons by the capillary force and its neck breaks. Bubble spends a longer time merging and leaving the whole structure in H=100 than that in H=20. The long retention of bubbles in the channel will hinder the replenishment of the cooling liquid, which has a negative effect on heat transfer.

4.4 Metal foam porosity effect

Considering that the combination of porosity and column affect the bubble resistance together, three hybrid structures with different porosity are selected for simulation. A higher porosity means smaller metal skeletons, resulting in low effective thermal conductivity and providing a bigger space for fluid and bubbles.

Fig. 17 shows the pool boiling curves for different porosities. The pool boiling heat transfer performance initially decreases with the increase in porosity. With the increase heat flux, pool boiling heat transfer performance at the porosity of 0.96 tends to be demonstrated. According to Xu [20], the turning porosity is connected to the shift of dominant factor from surface area to bubble escaping resistance. The results imply that the dominant factor is influenced by heat flux.

To investigate the influence of ε on bubble behaviors, the time evolution of bubble growth-departure frequency and bubble departure-escape frequency are obtained from t=20 000 to t=110 000. Fig. 18(a) shows the time evolution of bubble growth-departure frequency at different ε. The growth-departure frequency is defined as the reciprocal of the time duration from bubble formation

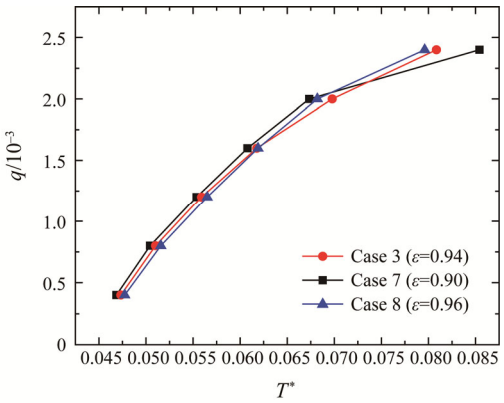

Fig. 17 Porosity effect on pool boiling curves

to bubble completely lifting off from the wall. It is noted that bubbles merge together before departure are treated as a single one. The growth-departure frequencies present little fluctuations at ε=0.96, while there are two nadir values in total at ε number of 0.90 and 0.94. The low frequency is connected to the bubble coalescence on the heating surface, because big bubbles stretch to fill the channels and are obstructed by the metal skeletons, thus are more difficult to rise up. Then, the unstable bubble residual is influenced by fresh water, thus causes a quick departure and a high frequency follows. Fig. 18(b) shows the time evolution of bubble departure-escape frequency at different ε. The departure-escape period denotes the duration from bubble leaving the channel bottom to bubble completely escaping from the hybrid structure surface. It is found that the bubble movement accelerates as time increases because of the temperature increasing on the heating surface. For average departure-escape frequencies during the statistical time period, $f_{\varepsilon=0.96}>$

$f_{\varepsilon=0.94}>f_{\varepsilon=0.90}$. Besides, the difference among departure-escape frequencies for different ε is more obvious than departure-escape frequencies. The fact implies that the heat transfer performance of hybrid structure with a low porosity is deteriorated due to high bubble escaping resistance.

4.5. Metal foam thickness effect

Fig. 19(a) shows the pool boiling curves of different n. It is found that the heat transfer performance of hybrid structures at n=2 is better than n=1. However, the heat transfer performance at n=3 is inferior to those at n=2 and n=1 with increasing heat flux. Similar to the decrease of porosity, increasing metal foam layer thickness means the increase of surface area which is the positive effect, and the increase of bubble escaping resistance which is the negative effect.

Fig. 19(b) shows the normalized heat flux q/A as a function of T^*. The heated surface area A is given by:

$$A = A_{\text{column}} + A_{\text{metal-foam}} \tag{31}$$

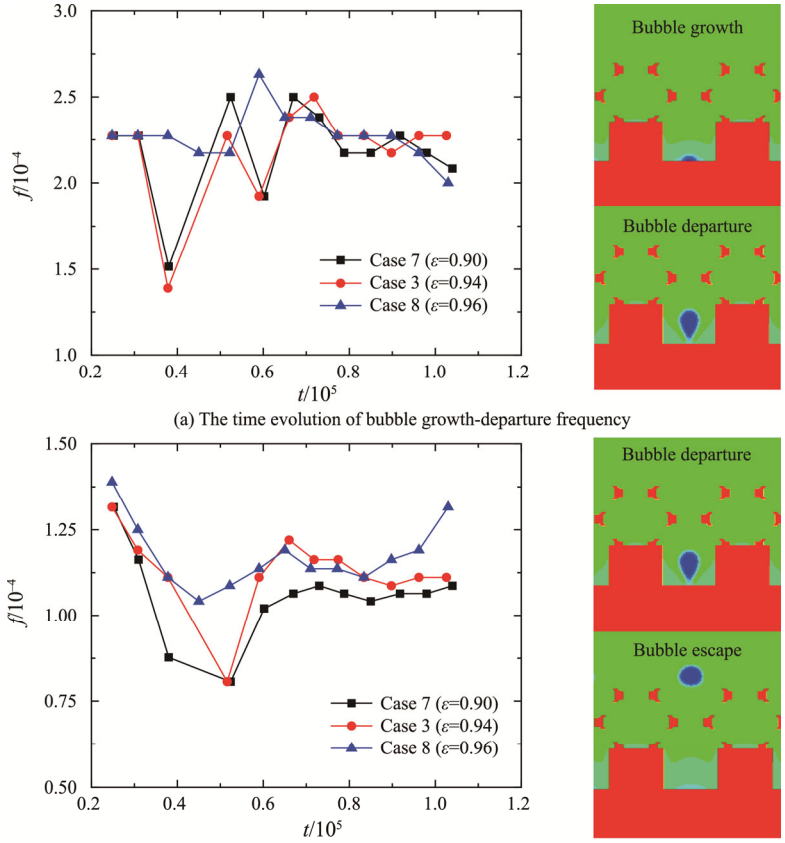

(a) The time evolution of bubble growth-departure frequency

(b) The time evolution of bubble departure-escape frequency

Fig. 18 Bubble motion frequency inside the hybrid structure (q=0.0016)

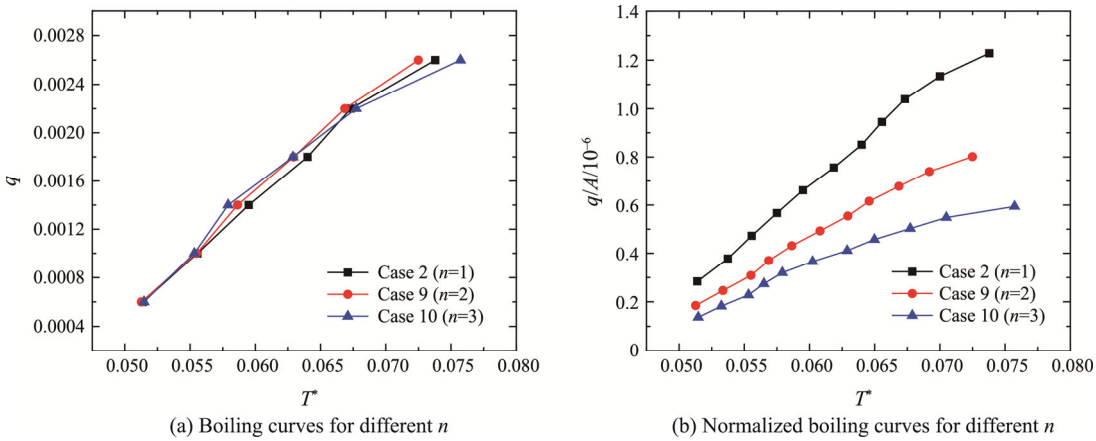

(a) Boiling curves for different n

(b) Normalized boiling curves for different n

Fig. 19 Thickness effect on pool boiling curves

where A_{column} is the surface of column and $A_{metal\text{-}foam}$ is the cross area of metal foam. It is found that the normalized heat flux q/A and normalized CHF decrease with the increase of thickness n. The result implies that the increase of n worse the pool boiling heat transfer performance per surface area. Bubble movement in metal foam is different from that in vertical channels. The effect of metal foam on bubbles is affected by the number and volume of bubbles. When bubbles are small, they can move freely inside the pores. When bubbles are larger than the pore size, they will be significantly hindered by the metal skeletons. Fig. 20 is a schematic diagram of force analysis when a large bubble is hindered by metal skeletons. The bubble in the flow field will be subjected to buoyancy force F_b, growth force F_g, evaporative momentum force F_M, surface tension F_σ, and contact pressure F_{cp}, friction force F_f and shear force F_τ from the metal skeletons. The evaporation momentum force is obtained from [38]:

$$F_M \sim \left(\frac{q}{h_{lv}}\right)^2 \frac{1}{\rho_V} \tag{32}$$

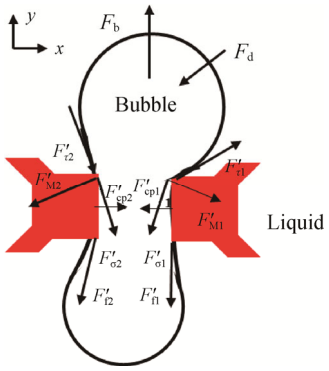

Fig. 20 The schematic diagram of bubble force in metal skeleton of hybrid structure

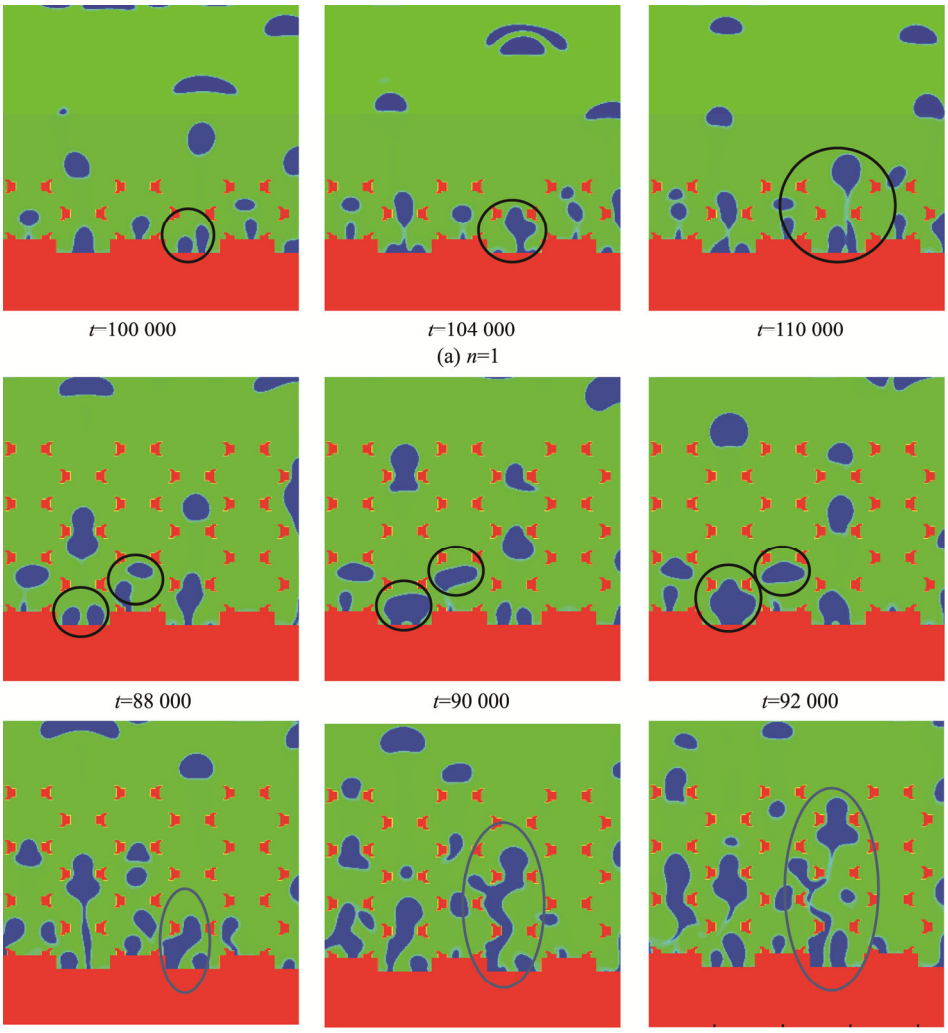

Fig. 21 Snapshots of boiling process (q=0.0024)

The growth force is given by [39]:

$$F_{\mathrm{g}}=\rho_{\mathrm{l}}\pi R(t)_{\mathrm{b}}^{2}\left[\frac{3}{2}c_{\mathrm{s}}R(t)'^{2}+R_{\mathrm{b}}R(t)''^{2}\right] \tag{33}$$

With the increase of heat flux, the evaporative momentum increases, which accelerates bubble growth and movement. At a high heat flux, numerous bubbles generate and rise up into the metal skeletons. Due to the increasing distance from the heating surface, the superheat of the skeletons decreases, thus reduces the latent heat transferred within the same period, bubble evaporation speed and the growth force [40]. However, due to the limited pore area, the growth force increases significantly, thus leading to bubble blocked in metal skeletons. During the process of bubbles moving upwards, the contact pressure, friction force and shear force promote bubble deformation and rupture.

Fig. 21(b) gives the bubbles behaviors concerning bubble merge, departure, deformation and burst of n=3 in the nucleation regime at q=0.0024. At high heat flux, many bubbles generate in the heating surface (t=88 000), merge in the pores of metal foam (t=90 000), are squeezed by the metal skeletons and deform (t=92 000). When bubbles coalesce into a big one (t=108 000), their departure becomes difficult. The vapor coverage forms on the fibers due to the bubble obstruction by metal skeletons (t=118 000). Then an amount of heat can be transferred from metal skeletons to bubbles. Finally, the bubble is split by the fibers and then the split parts slide through the inner-connected pores (t=122 000). Fig. 21 indicates that bubble behaviors in the hybrid structure with thicker metal foam layer are more complicated than those with thin foam layer. Xu et al. [41] and Yang et al. [42] also proved that pool boiling performance was influenced by foam thickness. Manetti et al. [10] concluded the influence of foam thickness on pool boiling. The thinnest has a smaller area that mainly influences the natural convection heat transfer, while metal foam with higher thickness has more nucleation sites and faster bubble growth frequency, leading to bubbles trapped in the pores.

5. Conclusions

Pool boiling heat transfer of column-metal foam hybrid structure is investigated by LBM. The influences of the hybrid structure parameters on heat transfer performance are investigated and the heat transfer mechanisms are revealed. Results imply that the square column-metal foam hybrid structures enhance boiling heat transfer effectively. The main conclusions are as follows.

(1) Ratio of column width to spacing has a significant influence on pool boiling heat transfer performance of the hybrid structure. At high heat fluxes, pool boiling heat transfer coefficient of the hybrid structure increases up to 25% with a W/D reduction from 5/3 to 1/3. However, at low heat fluxes, the heat transfer performance of the structure with the ratio of 3/5 is inferior to the other three structures with a HTC reduction from 0.15% to 3.4%.

(2) A hybrid structure with a higher column height is attributed to better heat transfer performance when heat flux is lower than 0.0022, and leads to a lower CHF due to bigger bubbles departure resistance and less nucleation sites.

(3) The effect of metal foam porosity and thickness on heat transfer performance of the hybrid structure is the competition between heating surface area effect and bubble escaping resistance effect. The hybrid structure with higher thickness has worse heat transfer performance per surface area and more complicated bubble behaviors.

Acknowledgments

This work is supported by the National Natural Science Foundation of China (Grant No. 52276075).

References

[1] Liang G., Mudawar I., Review of pool boiling enhancement with additives and nanofluids. International Journal of Heat and Mass Transfer, 2018, 124: 423–453.

[2] Kamel M.S., Lezsovits F., Enhancement of pool boiling heat transfer performance using dilute cerium oxide/water nanofluid: An experimental investigation. International Communications in Heat and Mass Transfer. 2020, 114: 104587.

[3] Modi M., Kangude P., Srivastava A., Performance evaluation of alumina nanofluids and nanoparticles-deposited surface on nucleate pool boiling phenomena. International Journal of Heat and Mass Transfer, 2020, 146: 118833.

[4] Yin J., Xiao X., Feng L., et al., Experimental investigation of pool boiling characteristics of surfactant solutions on bi-conductive surfaces. International Journal of Heat and Mass Transfer, 2020, 157: 119914.

[5] Etedali S., Afrand M., Abdollahi A., Effect of different surfactants on the pool boiling heat transfer of SiO_2/deionized water nanofluid on a copper surface. International Journal of Thermal Sciences, 2019, 145: 105977.

[6] Tian Z., Etedali S., Afrand M., et al., Experimental study of the effect of various surfactants on surface sediment and pool boiling heat transfer coefficient of silica/DI water nano-fluid. Powder Technology, 2019, 356: 391–402.

[7] Kumar N., Raza M.Q., Raj R., Surfactant aided bubble departure during pool boiling. International Journal of Thermal Sciences, 2018, 131: 105–113.

[8] Doran B., Zhang B., Walker A., et al., Experimental determination of the role of increased surface area in pool boiling from nanostructured surfaces. Experimental Thermal and Fluid Science, 2020, 111: 109956.

[9] Mehralizadeh A., Reza Shabanian S., Bakeri G., Effect of modified surfaces on bubble dynamics and pool boiling heat transfer enhancement: A review. Thermal Science and Engineering Progress, 2020, 15: 100451.

[10] Manetti L.L., Moita A.S.O.H., de Souza R.R., et al., Effect of copper foam thickness on pool boiling heat transfer of HFE-7100. International Journal of Heat and Mass Transfer, 2020, 152: 119547.

[11] Swain S., Swain A., Kar S.P., Influence of different surface coatings on pool boiling heat transfer enhancement: A brief review. Materials Today: Proceedings, 2020, 26: 1903–1907.

[12] Tang Y., Tang B., Li Q., et al., Pool-boiling enhancement by novel metallic nanoporous surface. Experimental Thermal and Fluid Science, 2013, 44: 194–198.

[13] Duan L., Liu B., Qi B., et al., Pool boiling heat transfer on silicon chips with non-uniform micro-pillars. International Journal of Heat and Mass Transfer, 2020, 151: 119456.

[14] Lei Z., Liu B., Xu P., et al., The pool boiling heat transfer and critical vapor column coalescence mechanism of block-divided microstructured surfaces. International Journal of Heat and Mass Transfer, 2020, 150: 119362.

[15] Li Z., Sarafraz M.M., Mazinani A., et al., Pool boiling heat transfer to CuO-H_2O nanofluid on finned surfaces. International Journal of Heat and Mass Transfer, 2020, 156: 119780.

[16] Liang G., Chen Y., Yang H., et al., Nucleate boiling heat transfer and critical heat flux (CHF) from micro-pit surfaces. International Journal of Heat and Mass Transfer, 2020, 152: 119510.

[17] Pi G., Deng D., Chen L., et al., Pool boiling performance of 3D-printed reentrant microchannels structures. International Journal of Heat and Mass Transfer, 2020, 156: 119920.

[18] Gouda R.K., Pathak M., Khan M.K., Pool boiling heat transfer enhancement with segmented finned microchannels structured surface. International Journal of Heat and Mass Transfer, 2018, 127: 39–50.

[19] Liu B., Yu L., Zhang Y., et al., Enhanced nucleate pool boiling by coupling the pinning act and cluster bubble nucleation of micro-nano composited surfaces. International Journal of Heat and Mass Transfer, 2020, 157: 119979.

[20] Xu Z.G., Qu Z.G., Zhao C.Y., et al., Experimental correlation for pool boiling heat transfer on metallic foam surface and bubble cluster growth behavior on grooved array foam surface. International Journal of Heat and Mass Transfer, 2014, 77: 1169–1182.

[21] Pastuszko R., Pool boiling heat transfer on micro-fins with wire mesh—Experiments and heat flux prediction. International Journal of Thermal Sciences, 2018, 125: 197–209.

[22] Jaikumar A., Kandlikar S.G., Enhanced pool boiling for electronics cooling using porous fin tops on open microchannels with FC-87. Applied Thermal Engineering, 2015, 91: 426–433.

[23] Jaikumar A., Kandlikar S.G., Enhanced pool boiling heat transfer mechanisms for selectively sintered open microchannels. International Journal of Heat and Mass Transfer, 2015, 88: 652–661.

[24] Gong S., Cheng P., Lattice Boltzmann simulation of periodic bubble nucleation, growth and departure from a heated surface in pool boiling. International Journal of Heat and Mass Transfer, 2013, 64: 122–132.

[25] Gong S., Cheng P., Numerical simulation of pool boiling heat transfer on smooth surfaces with mixed wettability by lattice Boltzmann method. International Journal of Heat and Mass Transfer, 2015, 80: 206–216.

[26] Chang X., Huang H., Cheng Y., et al., Lattice Boltzmann study of pool boiling heat transfer enhancement on structured surfaces. International Journal of Heat and Mass Transfer, 2019, 139: 588–599.

[27] Zhou P., Liu Z., Liu W., et al., LBM simulates the effect of sole nucleate site geometry on pool boiling. Applied Thermal Engineering, 2019, 160: 114027.

[28] Zhou P., Liu W., Liu Z., Lattice Boltzmann simulation of nucleate boiling in micro-pillar structured surface. International Journal of Heat and Mass Transfer, 2019, 131: 1–10.

[29] Macnamara R.J., Lupton T.L., Lupoi R., et al., Enhanced nucleate pool boiling on copper-diamond textured surfaces. Applied Thermal Engineering, 2019, 162: 114145.

[30] Surtaev A., Kuznetsov D., Serdyukov V., et al., Structured capillary-porous coatings for enhancement of heat transfer at pool boiling. Applied Thermal Engineering, 2018, 133: 532–542.

[31] Krishnan S., Murthy J.Y., Garimella S.V., Direct simulation of transport in open-cell metal foam. Journal of Heat Transfer, 2006, 128(8): 793–799.

[32] Boomsma K., Poulikakos D., Corrigendum for the paper: Boomsma K., Poulikakos D., On the effective thermal conductivity of a three-dimensionally structured fluid-saturated metal foam. International Journal of Heat and Mass Transfer, 2011, 54(1): 746–748.

[33] Calmidi V.V., Mahajan R.L., The effective thermal conductivity of high porosity fibrous metal foams. Journal of Heat Transfer, 1999, 121(2): 466–471.

[34] Qin J., Xu Z.G., Liu Z.Y., et al., Pore-scale investigation on flow boiling heat transfer mechanisms in open-cell metal foam by LBM. International Communications in

Heat and Mass Transfer, 2020, 110: 104418.
[35] Friz W., Maximum volume of vapor bubbles. Physic. Zeitschz., 1935, 36: 354–379.
[36] Zuber N., Nucleate boiling. The region of isolated bubbles and the similarity with natural convection. International Journal of Heat and Mass Transfer, 1963, 6(1): 53–78.
[37] Li L., Chen C., Mei R., et al., Conjugate heat and mass transfer in the lattice Boltzmann equation method. Physical Review E., 2014, 89: 0433084.
[38] Kandlikar S.G., Scale effects on flow boiling heat transfer in microchannels: A fundamental perspective. International Journal of Thermal Sciences, 2010, 49(7): 1073–1085.
[39] Zeng L.Z., Klausner J.F., Mei R., A unified model for the prediction of bubble detachment diameters in boiling systems-I. Pool boiling. International Journal of Heat and Mass Transfer, 1993, 36(9): 2261–2270.
[40] Huang R.L., Zhao C.Y., Xu Z.G., Investigation of bubble behavior in gradient porous media under pool boiling conditions. International Journal of Multiphase Flow, 2018, 103: 85–93.
[41] Xu J., Ji X., Zhang W., et al., Pool boiling heat transfer of ultra-light copper foam with open cells. International Journal of Multiphase Flow, 2008, 34(11): 1008–1022.
[42] Yang Y., Ji X., Xu J., Pool boiling heat transfer on copper foam covers with water as working fluid. International Journal of Thermal Sciences, 2010, 49(7): 1227–1237.